



Photocatalytic improvement of Mn-adsorbed $g\text{-C}_3\text{N}_4$

Weibin Zhang^a, Zhijun Zhang^{a,b}, Sangwoo Kwon^a, Fuchun Zhang^c, Boandoh Stephen^d, Ki Kang Kim^d, Ranju Jung^e, Sera Kwon^a, Kwun-Bum Chung^a, Woochul Yang^{a,*}

^a Department of Physics, Dongguk University, Seoul, 04620, Republic of Korea

^b School of Materials Science and Engineering, Shanghai University, Shanghai, 200072, PR China

^c College of Physics and Electronic Information, Yanan University, Yanan, 716000, PR China

^d Energy and Materials Engineering Department, Dongguk University, Seoul, 04620, Republic of Korea

^e Department of Electrical and Biological Physics, Kwangwoon University, Seoul, 01897, Republic of Korea



ARTICLE INFO

Article history:

Received 27 October 2016

Received in revised form

27 December 2016

Accepted 13 January 2017

Available online 15 January 2017

Keywords:

Density functional theory

$g\text{-C}_3\text{N}_4$

Mn-adsorption

Photocatalyst

ABSTRACT

This study employed experimental results and theoretical calculations to investigate Mn-adsorbed $g\text{-C}_3\text{N}_4$ as a potential photocatalyst with high efficiency. Mn was chosen as the incorporating element, because among the 3d transition metals it exhibits the highest binding energy and most suitable band edge positions. The photocatalytic efficiency of Mn-adsorbed $g\text{-C}_3\text{N}_4$ is 3 times higher than that of pristine $g\text{-C}_3\text{N}_4$. Although small variations in the phase and surface morphology were observed, which were confirmed to not be the determining factors to improve efficiency. The factors that affect the high photocatalytic efficiency are therefore the electronic structure, optical absorption, and band edge variations after Mn-adsorption. The Mn atoms stably are bonded with N atoms, due to the strong absorption energy and ionic bond. Moreover, reduction of the $g\text{-C}_3\text{N}_4$ band gap after Mn-adsorption results in a red shift of the absorption band edge. The half-filled Mn 3d state introduces impurity states into the forbidden band gap, which will increase the life time of charge carriers. In addition, the up-shifting of band edges of Mn-adsorbed $g\text{-C}_3\text{N}_4$ leads to inhibition of the electron-hole recombination. As a consequence, the photocatalytic efficiency of Mn-adsorbed $g\text{-C}_3\text{N}_4$ is enhanced due to the combination of the aforementioned effects.

© 2017 Elsevier B.V. All rights reserved.

1. Introduction

Recently, intense research activities have sought suitable materials as photocatalysts for splitting water or environmental pollutants by using solar energy. The optimal material should not only have strong light absorption ability, suitable band gap, and redox potential, but also be stable, non-toxic, abundant, and easily processable into a desired shape. Unfortunately, most semiconductors do not meet all of these criteria. TiO_2 has been the dominant material used, but its band gap is too wide (3.26 eV) to efficiently absorb visible light [1]. In recent years, growing interest has focused on the non- TiO_2 -based catalysts. However, the present achievements are still far from the ideal materials [2,3]. Most of the available catalysts are active only under UV irradiation, while others that are capable of absorbing visible light are not stable during the reaction process [4]. Recently, graphitic carbon nitride ($g\text{-C}_3\text{N}_4$) materials have been explored for various applications, especially

in visible light photocatalysis, owing to their large specific surface area, short diffusion length, high chemical stability, and appealing electronic structure, with a band gap of 2.70 eV that is suited to absorbing blue light [5,6]. In addition, the high nitrogen content in $g\text{-C}_3\text{N}_4$ plays an important role in boosting photoelectric conversion efficiency, as the nitrogen atoms affect the spin density and charge distribution of carbon atoms, inducing activated regions on the surface [7].

On the other hand, the photocatalytic efficiency of $g\text{-C}_3\text{N}_4$ under visible light has been found to be low, absorbing only 0.1% of the irradiated visible light [8]. Further study has ascribed the low activity to many factors, for example the high excitation energy determined by the band gap energy, low charge mobility originating from the nature of the polymer, low specific surface area (2–10 m^2/g), and insufficient sunlight absorption [8]. Recently, some effective methods such as nanostructure modification [9] and the introduction transition metals (TMs) or nanoparticles into $g\text{-C}_3\text{N}_4$ [10,11] were reported to improve the photocatalytic activity of $g\text{-C}_3\text{N}_4$ under visible light. Also, chemical doping with non-metallic elements or deposition with metal atoms is an alternative strategy to modify the electronic structures as well as their surface

* Corresponding author.

E-mail address: wyang@dongguk.edu (W. Yang).

properties to improve their performance [12]. Among all doping elements exploited so far, the 3d *TM*s have widely been employed, since the *d*-orbitals of *TM*s hybridize with the *p*_π-orbitals of the g-C₃N₄ framework, and meanwhile decrease the band gap of *TM*s-incorporated g-C₃N₄. Importantly, most of these materials possess magnetic properties, which is important to the photocatalyst recycling process [13].

To select properly doping/adsorbing *TM* atoms, some key factors such as the stability, carrier density, and synthesis should be considered. First, the stability is important for photocatalysts. The binding energy after incorporation/adsorbed can be applied to evaluate the stability. The small or negative binding energy implies that these *TM* atoms have a tendency to segregate and ultimately form metal clusters in the catalyst. Among the *TM*s-adsorbed g-C₃N₄ systems previously investigated, the binding energy of Mn is the strongest (i.e., Mn is 4.48 eV, Cr is 3.65, Zn is -1.40, etc.). Second, the carrier density of the g-C₃N₄ system after *TM*s-incorporation/adsorbed is one of the key factors for the photocatalyst, as higher carrier density materials make the photogenerated e⁻/h⁺ pair easier to migrate onto the surface. Among all the *TM*s investigated, the electron carrier density of the Mn-adsorbed system is the highest ($5.0 \times 10^{13} \text{ cm}^{-2}$) [13]. Finally, the Mn-adsorbed systems have been easily and successfully synthesized by mixing MnCl₂ with substrate materials [14,15]. To the best of our knowledge, there is no report on the photocatalytic properties of Mn-adsorbed g-C₃N₄. Therefore, systematic investigation of the electronic structure and optical properties of Mn-adsorbed g-C₃N₄ is urgent and important for photocatalytic applications.

This report employed experimental and theoretical methods to examine the photocatalytic activity of Mn-adsorbed g-C₃N₄. Our results indicate that Mn is the most promising adsorbed element among all of the 3d *TM*s. XRD, XANES, XPS, Raman and SEM, TEM measurements were performed to determine the morphology and phase change. The photocatalytic efficiency was also studied, and was found to be significantly improved. The results show that the chemical compositional variation is the contributing factor to the optical absorption range extension and band edge shift, which results in the improvement in photocatalytic efficiency.

2. Experimental and computational methods

2.1. Sample preparation

The g-C₃N₄ powders were synthesized directly by heating melamine in a semi-closed system according to the literature [16]. First, 10 g of melamine was heated in a muffle furnace from room temperature to 520 °C with a rate of 4 °C/min. After calcination at 520 °C for 2 h, the as-prepared g-C₃N₄ was naturally cooled to room temperature, and ground to powder. The Mn-adsorbed g-C₃N₄ powders were synthesized by the following process. 1 g of g-C₃N₄ and different amounts of MnCl₂ were mixed with 20 mL ethanol, and stirred for 2 h at 80 °C. The amounts of MnCl₂ were 0.01, 0.05, 0.10, 0.20, 0.30 and 0.40 g, and were named as Mn1/CN, Mn5/CN, Mn10/CN, Mn20/CN, Mn30/CN and Mn40/CN, respectively. These mixed solutions were maintained at 80 °C to remove ethanol. Finally, the remaining powders were kept at 600 °C for 4 h.

Rhodamine B (RhB) dye was used to test the photocatalytic activities of samples. Photocatalytic reaction was performed in a Pyrex reactor. The catalysts (0.20 g) were dispersed in RhB aqueous solution (100 mL, 4 mg/L). The light irradiation system contained a 300 W Xe-lamp with a cut-off filter L42 for visible light, and a water filter to remove heating effects. Before irradiation, the suspensions were first sonicated for 5 min, and were then shaken overnight in the dark to establish adsorption-desorption equilibrium. During the irradiation process, 5 mL of suspension were collected every

20 min, and centrifuged twice at 10,000 rpm for 5 min each time to remove photocatalyst nanoparticles. The concentration of RhB in supernatant was then analyzed by Agilent 8451 spectrometry at 552 nm.

2.2. Characterization

Raman spectra were collected by Renishaw micro-Raman spectrometry with an excitation laser at 785 nm. The X-ray diffraction (XRD) patterns were determined by HUBER Imaging Plate Guinier Camera G670 (Cu K α_1 radiation, $\lambda = 1.54056 \text{ \AA}$, Ge monochromator) from 5.0 to 100° with a step of 0.005°. Size, shape and element mapping of the samples were characterized by field emission scanning electron microscopy (FE-SEM, S-4800 Hitachi) operating at 15 kV. The X-ray photoelectron spectroscopy (XPS) was obtained by Thermo ESCALAB 250X electron spectrometry using 150 W Al K α X-ray sources. The absorption spectra were recorded by Cary 5000 spectrophotometry (Varian Inc., USA) with a Xe flash lamp. The emission and excitation spectra of the samples were measured by Perkin Elmer LS 50B spectrophotometry equipped with Xe flash lamp. The excitation and emission slits were set at 15 nm. All of the measurements were carried out at room temperature. The X-ray absorption near-edge structure (XANES) spectra were collected in fluorescence mode at room temperature using the facility at the 1D beam line (for Mn *K*-edge) of Pohang Accelerator Laboratory (PAL), Korea. The specific surface areas of the catalysts were determined by N₂ adsorption-desorption measurement at -196 °C employing the Brunauer-Emmett-Teller (BET) method (Autosorb-iQ, Quantachrome). High-resolution transmission electron microscopy (HR-TEM) images were obtained on a JEM-2010F electron microscope with an acceleration voltage of 300 kV.

2.3. Computational details

First principles calculations based on density functional theory (DFT) with a plane-wave pseudo-potential basis were performed using the VASP (Vienna Ab initio Simulation Package) code [17]. Since the local density approximation (LDA) typically overestimates the adsorption energy while underestimating the equilibrium atomic distances of the model system [18], the uniform generalized gradient approximation (GGA) with the Perdew–Burke–Ernzerhof (PBE) method was applied to structural optimization [19]. It is well known that partially filled *d*-orbital containing systems cannot be accurately described by using only the GGA function; thus the GGA + *U* method was used, as proposed by Dudarev [20]. The on-site Coulomb interaction parameter *U* and the exchange parameter *J* are combined into a spherically averaged, single effective interaction parameter *U*–*J* (*U*_{eff}), which does not depend on their individual values. The *U*_{eff} for the *TM*s are applied with the recommended values provide by Yang Yu et al. [21].

The cut-off energy is set to be 400 eV for plane-wave expansion of electron wave functions of both carbon and nitrogen atoms. The criteria for convergence in energy and force are 10⁻⁵ eV and 0.05 eV/Å, respectively. The first Brillouin-zone was sampled with a 3 × 3 × 1 *k*-point grid. Also, higher cut-off energy and *k*-point were tried, but there was no marked improvement. These parameters were applied to optimize the g-C₃N₄ unit cell until the deviation was no more than 5%, compared with the unit cell obtained from experimental and other theoretical results, as shown in Table S1. The electronic structures and optical properties were calculated using the hybrid density functional HSE06 (Heyd-Scuseria-Ernzerhof) [22] hybrid function, which replaced the slowly decaying long-ranged part of the Fock exchange by the corresponding density functional counterpart. The modeled g-C₃N₄ (001) 2 × 2 surface was a slab with five atomic layers, which was separated from a 15 Å thick vacuum region. The thicknesses of the

slabs and vacuum region were set to be sufficient to avoid interaction between the replicas. The surface was then adsorbed with Mn, and relaxed to attain stable structures.

3. Results and discussion

3.1. The transition metals-adsorbed $g\text{-C}_3\text{N}_4$

To improve the photocatalytic efficiency, investigations of the un-fulfilled 3d TMs-adsorbed $g\text{-C}_3\text{N}_4$ were performed to choose the optimum element. As is well known, these TMs on the top of $g\text{-C}_3\text{N}_4$ are quite mobile in nature and form clusters due to strong $d\text{-}d$ interaction [23]. Therefore, we first initiate investigation of the binding energy of TM-adsorbed $g\text{-C}_3\text{N}_4$. The average binding energy is calculated by using the following formula [13],

$$E_b = E_{CN} + E_{TM} - E_{TM/CN}, \quad (1)$$

where E_{CN} and E_{TM} are the energy of bare $g\text{-C}_3\text{N}_4$ and TM atom in its bulk phase, respectively, and $E_{TM/CN}$ denotes the total energy of TM-adsorbed $g\text{-C}_3\text{N}_4$.

Table 1 shows that the binding energies of Sc, Ti, V, Cr, Mn and Fe-adsorbed $g\text{-C}_3\text{N}_4$ is positive, which means that these TM-adsorbed $g\text{-C}_3\text{N}_4$ systems are stable. However, negative binding energies for Co and Ni indicate that these TM atoms have a tendency to segregate and form metal clusters. It is noteworthy that the binding energy of Mn is the highest, as the crystal ionic radius of divalent Mn^{2+} is the largest among the other divalent TM^{2+} ions [24].

Since the positions of the band edge are important for photocatalytic efficiency improvement, the band edges of the TMs-adsorbed $g\text{-C}_3\text{N}_4$ are calculated to help choosing the appropriate TMs. Before the band edge calculations, the work function need to be calculated firstly, as the relative positions of band edges usually change with the Fermi level. Fig. 1(a) and (b) show the calculated work functions of the pristine $g\text{-C}_3\text{N}_4$ and TM-adsorbed $g\text{-C}_3\text{N}_4$. Physisorption of the atoms/molecules on the material surfaces may give rise to a decrease of the work function, since the Pauli repulsion between the molecular and surface electrons decreases the surface dipole. Chemisorption also can lead to variation in the work function, and even to counterintuitive results [25]. Thus, it is crucial to investigate the relationship between the work function and the differently adsorbed TMs. The work function (Φ) is formally defined as [26]:

$$\Phi = D - E_F \quad (2)$$

where D is the potential energy at an infinite distance from the system, and E_F is the Fermi level. Based on the work function calculations, we can obtain the Fermi levels and band edges of TMs-adsorbed $g\text{-C}_3\text{N}_4$ systems, which will be discussed as follows.

The energy positions of the valence band edge (E_{VB}) and conduction band edge (E_{CB}) of $g\text{-C}_3\text{N}_4$ are then calculated according to the following equations [27]:

$$E_{VB} = \chi - E_e + 0.5E_g \quad (3)$$

$$E_{CB} = E_{VB} - E_g \quad (4)$$

where χ is the absolute electronegativity of the semiconductor. In essence, the Fermi level can be obtained from the absolute electronegativity [28] and the calculated work function. E_e is the energy of free electrons on the hydrogen scale (4.50 eV). E_g is the band gap of the semiconductor, which is calculated be 2.70 eV for $g\text{-C}_3\text{N}_4$. Fig. 1(c) shows the E_{VB} and E_{CB} of various TMs-adsorbed $g\text{-C}_3\text{N}_4$ calculated from Eqs. (2)–(4). Only Cr, Mn and Fe-adsorbed $g\text{-C}_3\text{N}_4$ are suitable for photocatalysts. In particular, the E_{VB} of Mn-adsorbed $g\text{-C}_3\text{N}_4$ is the closest to the $\text{O}_2/\text{H}_2\text{O}$ redox line. It is well known that the smaller the potential distance between the E_{VB} and $\text{O}_2/\text{H}_2\text{O}$ redox line, the easier it is for the holes to interact with H_2O , resulting in inhibition of the electron-hole recombination.

To sum up, Mn is the most suitable element among the 3d TMs applied to adsorb $g\text{-C}_3\text{N}_4$ as photocatalyst. There are two reasons for this: first, the binding energy is the strongest among the TMs investigated, which means the Mn-adsorbed $g\text{-C}_3\text{N}_4$ is the most stable; second, among the investigated TMs the E_{VB} of Mn-adsorbed $g\text{-C}_3\text{N}_4$ is the closest to the $\text{O}_2/\text{H}_2\text{O}$ redox line, resulting in better photocatalytic efficiency.

3.2. The photocatalytic activity improvement

The photocatalytic efficiency of the Mn-adsorbed $g\text{-C}_3\text{N}_4$ is further investigated. It is well known that dyes are important organic compounds and have been widely applied in textiles, food additives. Also, they are often regarded as environmental contaminants. Thus we evaluated the photocatalytic activity of the Mn-adsorbed $g\text{-C}_3\text{N}_4$ by monitoring the degradation of RhB [29] – an azo dye – under solar light. Fig. 2(a) shows the temporal adsorption spectra of the RhB solution exposed to visible light in the presence of Mn1/CN. RhB in water showed a strong absorption band centered at 554 nm. Under solar light illumination, there is a decrease in maximum absorbance, and blue shift in the maximum absorption with increasing exposure times. The decrease of maximum absorbance is considered to be cycloreversion, and the blue shift in the maximum absorption could be attributed to *N*-deethylation [30]. The pink color of the solution disappears completely after 160 min of irradiation (as per the inset of Fig. 2(a)), indicating that photocatalysis destroyed the chromophoric structure of the dye.

According to the previous reports, the decomposition of RhB can be assigned to a pseudo-first-order kinetics reaction with a simplified Langmuir-Hinshelwood model when C_0 is very low [31]. That is,

$$\ln(C/C_0) = -kt \quad (5)$$

where C is the concentration of RhB at time t , and C_0 is the initial concentration of RhB; k is the apparent first-order kinetics rate constant, which reflects the photocatalytic efficiency. Fig. 2(b) shows that photocatalytic degradation of RhB under visible light irradiation over RhB solution without/with pristine and Mn-adsorbed $g\text{-C}_3\text{N}_4$. The photocatalytic efficiency of Mn1/CN (0.019 min^{-1}) is a little higher than that of pristine $g\text{-C}_3\text{N}_4$ (0.017 min^{-1}), while that of Mn20/CN (0.047 min^{-1}) is 3 times of that for the pristine $g\text{-C}_3\text{N}_4$. Meanwhile, the efficiency decreases with Mn concentration increases higher than 20%. Obviously, the photocatalytic efficiency of $g\text{-C}_3\text{N}_4$ is improved after Mn-adsorption, and the optimum concentration of adsorbed Mn is 20%. In addition, to exclude the direct oxidation of RhB dyes, the photo-degradation of colorless pollutant (phenol) under visible light irradiation was examined to confirm the photocatalytic activity improvement by Mn-adsorbed $g\text{-C}_3\text{N}_4$, as shown in Fig. S2. We obtained the similar results, where the photocatalytic efficiency of Mn20/CN (0.0035 min^{-1}) is 2 times of that for the pristine $g\text{-C}_3\text{N}_4$ (0.019 min^{-1}).

It is well known that the popular efforts to improve the activity can be categorized into four approaches. The first approach is inter-layer engineering between two or more materials, such as changing the interfacial states, or making a built-in field. The second approach is phase and crystal facet engineering, as different phases and crystal planes show different catalytic activity. The third approach is micro-structural engineering, such as changing the surface/volume ratio, crystallinity, or surface morphology. The fourth approach is chemical composition engineering, which in fact is variation of the electronic states, conductivity, and optical properties. For example, many researchers have successfully doped or adsorbed some metal atoms or nanoparticles in the photocatalysts, which aids the electron-hole separation, or accelerates the migration of electron-hole pairs [32]. The first approach is not the key point in our work, as the particles are applied as catalyst, and do

Table 1

The calculated binding energy (E_b) of different TMs-adsorbed $g\text{-C}_3\text{N}_4$ systems, and the ionic radii (r) of divalent TM atoms.

Ions	Sc	Ti	V	Cr	Mn	Fe	Co	Ni
E_b (eV)	1.10	1.77	1.06	0.77	1.96	0.07	-0.41	-0.38
r (Å)	0.88	0.81	0.93	0.94	0.97	0.92	0.88	0.83

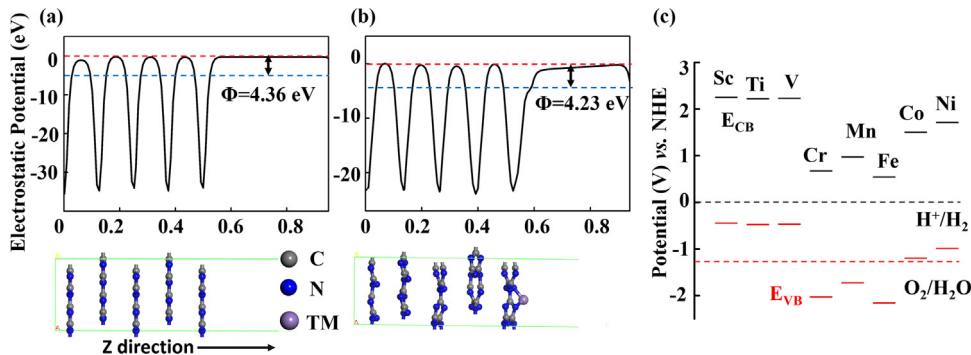


Fig. 1. (a) The electrostatic potential profile for pristine $g\text{-C}_3\text{N}_4$ along the z-axis, (b) the electrostatic potential profile for 1 TM-adsorbed $g\text{-C}_3\text{N}_4$ along the z-axis, and (c) the band edge positions of different TM-adsorbed $g\text{-C}_3\text{N}_4$. The work function (Φ) is defined as the difference between the vacuum energy (D) and the Fermi energy (E_F).

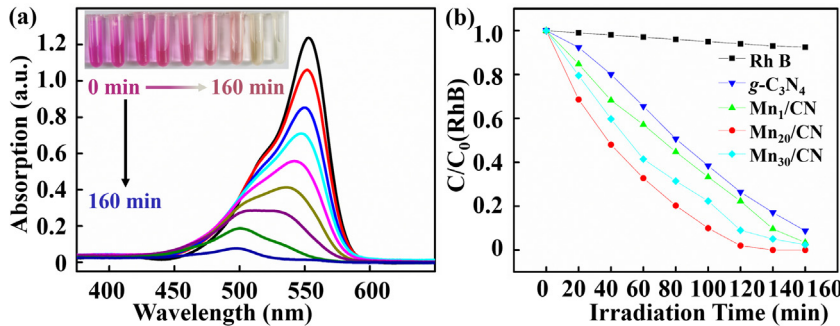


Fig. 2. (a) The temporal absorption spectrum changes of RhB solution during visible light irradiation in the presence of Mn1/CN. Inset shows a photo of the degradation of RhB solution. (b) the photocatalytic degradation of RhB solution, and $g\text{-C}_3\text{N}_4$, Mn1/CN, Mn20/CN, Mn30/CN mixed RhB solutions.

not include hybrid materials in our work. Therefore, the remaining approaches were considered to find the key factors to improve the photocatalytic efficiency by combining experimental and calculation method.

3.3. The phase, particle size and surface morphology changes with Mn concentration

The phase, particle size, and surface morphology changes are characterized by Raman, XRD, SEM, and EDS (energy-dispersive) element mapping, respectively. Fig. 3 shows the Raman spectra of pristine and Mn-adsorbed $g\text{-C}_3\text{N}_4$. The spectra confirm that the layered $g\text{-C}_3\text{N}_4$ is successfully derived from melamine, and the crystallization state of $g\text{-C}_3\text{N}_4$ remains after the mild chemical doping method [33]. The peaks at around 1231 cm^{-1} are ascribed to the $=\text{C}$ (sp^2) bending vibration, which shifts from 1231 cm^{-1} for pristine $g\text{-C}_3\text{N}_4$ to 1216 cm^{-1} for Mn20/CN. The blue shift can be attributed to the distortion of layers. The peaks at 771 and 706 cm^{-1} are assigned to the layer-layer deformation vibration, or correlation vibrations induced by the layer-layer vibrations. The ratio of peak heights between 771 and 706 cm^{-1} (I_{771}/I_{706}) reflects the average thickness changes. The I_{771}/I_{706} of pristine $g\text{-C}_3\text{N}_4$ is 0.17, and it increases to 0.43 for Mn20/CN. The increasing ratios infer the average bulk thickness decrease [33].

To confirm the Raman results, XRD is performed to investigate the crystallization state and cell parameters of the Mn-adsorbed $g\text{-C}_3\text{N}_4$. Fig. 4(a) shows that the peaks locate at around 27.5°

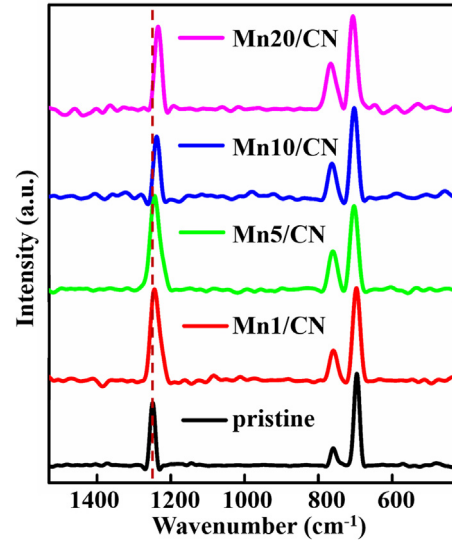


Fig. 3. Raman spectra of the pristine and Mn-adsorbed $g\text{-C}_3\text{N}_4$ with different Mn concentrations (785 nm laser).

corresponding to the (002) stacking layered structure (JCPDS: 87-1526). Fig. 4(b) shows that the peaks shift from 27.5° (pristine $g\text{-C}_3\text{N}_4$) to 27.8° (Mn20/CN), indicating that the corresponding interlayer spacing decreases. To further confirm the speculation,

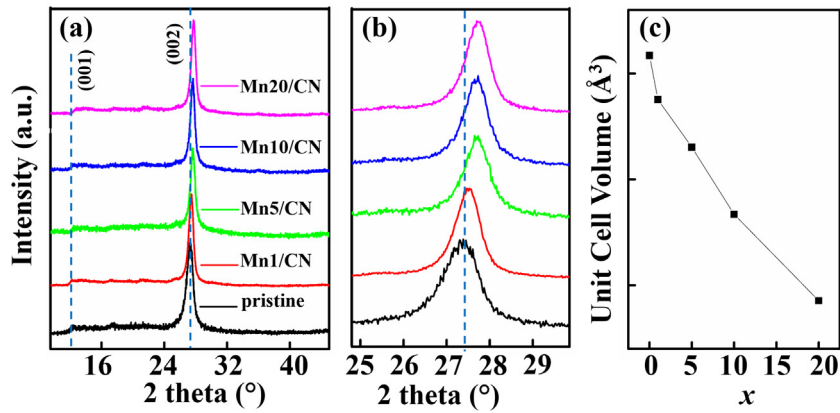


Fig. 4. (a) XRD patterns of pristine and different Mn-adsorbed g-C₃N₄, (b) a closer view of the (002) peak, and (c) the Mn concentration dependence of unit cell volume for Mn-adsorbed g-C₃N₄. x represents Mn concentration of the Mn1/CN, Mn5/CN, Mn10/CN, Mn20/CN samples.

the cell parameters of Mn-adsorbed g-C₃N₄ are calculated from the XRD indexing software package Fullprof [34]. Fig. 4(c) shows that the unit cell volumes of Mn-adsorbed g-C₃N₄ decrease with Mn concentration increases. Therefore, the XRD patterns confirm the Raman results that the layered g-C₃N₄ is successfully synthesized from melamine, and the particle size of Mn-adsorbed g-C₃N₄ decreases.

The microstructure of pristine and Mn-adsorbed g-C₃N₄ was examined via TEM analysis. Fig. 5 shows TEM images of pristine and Mn-adsorbed g-C₃N₄ as well as the associated SAED patterns. The TEM image of the pristine g-C₃N₄ indicates the well distributed slices like randomly oriented graphene-like layers (Fig. 5(a)). In the HR-TEM image (Fig. 5(b)), it is hard to observe a clear lattice fringe of pristine g-C₃N₄ because the g-C₃N₄ system is a semi-crystallized material. However, the FFT image shows 18 obvious dots, which resemble three different g-C₃N₄ layers (every 6 dots are in the same ring), as shown in the inset of Fig. 5(b). In addition, the image reconstructed by filtering in the frequency domain, which is the uniformed triazine structures in Fig. 5(c).

There is no obvious change in Mn20/CN sample in TEM and HR-TEM, as shown in Fig. 5(d) and (e). It is of note that the existence of particles in the Mn-adsorbed g-C₃N₄ can be excluded out. The FFT images shows 18 dots like g-C₃N₄, shown in the inset in Fig. 5(e). However, the distance between opposite dots increased, indicating a decrease of the interlayer distance. In addition, FFT images show triazine units structure in the pink ring region and partially modified structures in the yellow ring region. The variation of triazine structure of Mn-adsorbed g-C₃N₄ might be due to Mn adsorption on the g-C₃N₄ surface.

The interlayer distance of the pristine g-C₃N₄ is calculated to be 3.22 Å from the SAED patterns (Fig. 5(g)), which is in accordance with a previous report [35]. However, the interlayer distance of the Mn20/CN is decreased to be 2.07 Å (Fig. 5(h)). Comparing with XRD results, the SAED pattern of the Mn20/CN is in good agreement with the inter-planar spacing of (002) plane. The tendency of interlayer distance change after Mn adsorption is in agreement with Raman and XRD results, and also can be demonstrated by the calculation (The electrons transfer from Mn to g-C₃N₄, leading to a strong π - π stacking). Conclusively, there is no particle for Mn-adsorbed g-C₃N₄ and the interlayer spacing decreases after Mn-adsorption.

Typical SEM and EDS element mapping of g-C₃N₄ systems are then investigated. Fig. 6(a) shows the SEM image of pristine g-C₃N₄, which reveals the g-C₃N₄ samples to be composed of irregularly curved layers. These layers are packed in a random way, resulting in porous structure. Fig. 6(b) illustrates the SEM of the Mn20/CN, which is also composed of curved layers. There is no obvious variation in surface morphology after Mn-adsorption, which

implies that the introduction of Mn atoms does not influence the surface morphology. The EDS element mapping based on the scan area of Fig. 6(c) is also performed. The spatial resolution of EDS is 0.2–1.0 μm^3 , and the distribution and relative proportion (intensity) of the defined elements are mapped over the scanned area. The X-ray detector axis is at an angle to the horizontal plane (a typical and exact value of the X-ray detector in our measurement was 40°). Using the absorption coefficients computed from Heinrich's parameterization, one can find that the X-ray has only about 8% probability of reaching the surface, and thus actually arriving at the detector. Therefore, the X-ray signals from island parts are easier to arrive at the detector, while those from the hollow parts are difficult, as shown in the dotted red and orange rings of Fig. 6(d). Fig. 6(d) and (e) show the elemental mappings of C and N atoms. They reveal that the C and N atoms appear to be distributed across the bulk structure. Compared with the case of C and N mappings, the mappings of Mn indicates that the Mn atoms are not distributed in the bulk, as shown in Fig. 6(f). Therefore, the Mn atoms are uniformly distributed only on a small portion of particle surface, which is consistent with other reports [36].

Since the surface area of catalytic materials is another important factor in catalytic activity, the measurement of surface areas of g-C₃N₄ systems are carried out by BET method, as tabulated in Table 3. After Mn adsorption on the g-C₃N₄, the surface areas increased less than 11%, which probably is not enough to improve the photocatalytic efficiency. In addition, the total pore volume and average pore width of the Mn-adsorbed g-C₃N₄s changed irregularly. Therefore, there is no significant change in the surface area, pore volume, and average pore width after Mn adsorption on the g-C₃N₄, which means that the parameters related to the surface of Mn-adsorbed g-C₃N₄ are not the key factors for the photocatalytic efficiency improvement.

Accordingly, the DFT calculation models are set up, and theoretical calculations are performed herein to understand the mechanisms at the atomic level. Since Mn atoms are adsorbed on the first few layers, and most of the Mn are on the particle surface, the g-C₃N₄ system with Mn-adsorbed on the surface is chosen as the calculation model. Fig. 7(a) shows the top view of a monolayer of g-C₃N₄, which is chosen to show the different positions of Mn atom. There are five possible sites for Mn-adsorbed g-C₃N₄: the triangular N hole (T_t), the center of the hexagonal ring (H_t), the top of N1 (N1_t), the top of N2 (N2_t), and the top of C (C_t). N1 and N2 are N atoms with sp^2 (coordination number of 2) and sp (coordination number of 3) hybridization, respectively. Fig. 7(b) is the side view of our model, and the atomic ratio of 1, 2, 3, and 4 Mn-adsorbed g-C₃N₄ are 0.71, 1.41, 2.10, and 2.77 at.%, respectively. After Mn-adsorbed, the average interlayer distance decreases from 3.82 to 3.29 Å, which

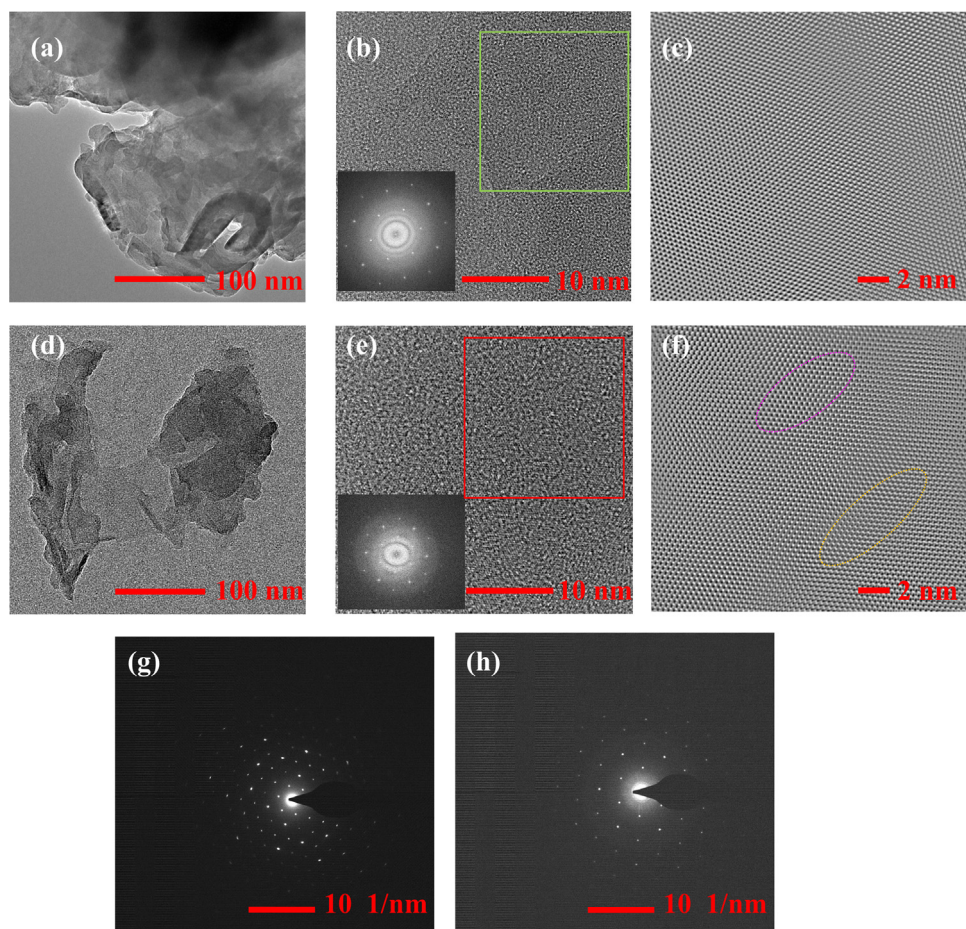


Fig. 5. (a) TEM image at different magnifications of (a-c) pristine $g\text{-C}_3\text{N}_4$ and (d-f) of Mn20/CN . The insets of (b) and (e) indicate FFT patterns in the green and red box for each image. (c, f) reconstructed images after filtering in the frequency domain to remove noise. (g, h) the SAED pattern of pristine $g\text{-C}_3\text{N}_4$ and Mn20/CN , respectively. (For interpretation of the references to colour in this figure legend, the reader is referred to the web version of this article.)

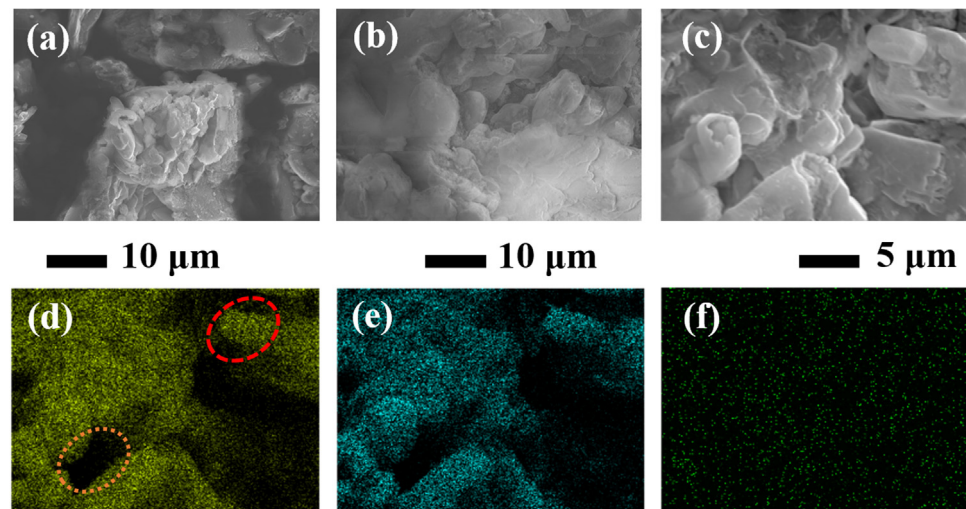


Fig. 6. SEM images and EDS element mapping. (a) and (b) are SEM image of the pristine $g\text{-C}_3\text{N}_4$ and the Mn20/CN samples, respectively; (c) is SEM image for a sketch of the sample in EDS element mapping analysis; and (d), (e) and (f) are element mappings of C, N and Mn, respectively.

is consistent with the experimental results. With Mulliken charge population analysis, the average charges on Mn are 1.36, 1.00, 0.55, and 0.53 $|\text{e}|$ for 1, 2, 3, and 4 Mn-adsorbed $g\text{-C}_3\text{N}_4$, respectively. It turns out that the decrease of interlayer distance originates from the Mn atoms donate electron to $g\text{-C}_3\text{N}_4$, inducing a strong $\pi\text{-}\pi$ stacking between layers (i.e. a stronger Van der Waals interaction).

To sum up, there is no significant change of the phase and surface morphology after Mn-adsorption. It indicates that the phase and surface morphology are not responsible for the photocatalytic efficiency improvement. Meanwhile, the average size of Mn-adsorbed $g\text{-C}_3\text{N}_4$ particles decreases a little. The size decrease is obviously not strong enough to improve the surface-to-volume ratio, and thus to

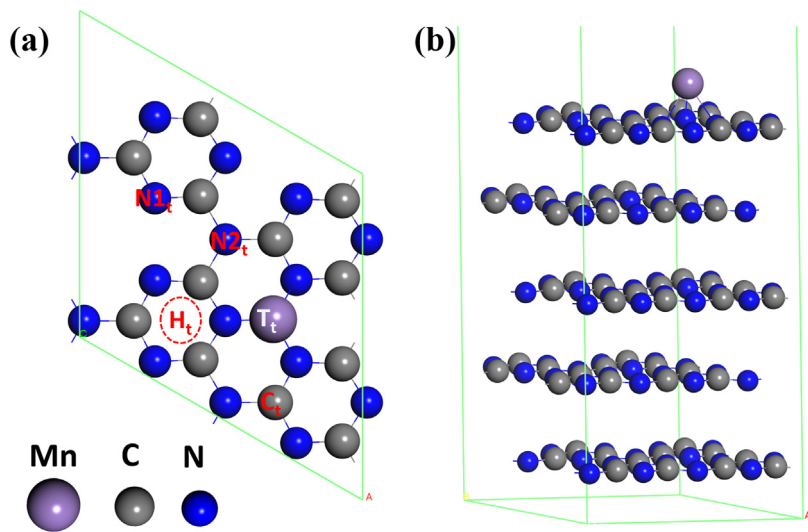


Fig. 7. (a) Side view of Mn-adsorbed g-C₃N₄. (b) Top view and possible doping sites of Mn atoms on g-C₃N₄: triangular N pore (T_t), hexagonal rings (H_t), top of N1 (N1_t), top of N2 (N2_t), and top of C (C_t).

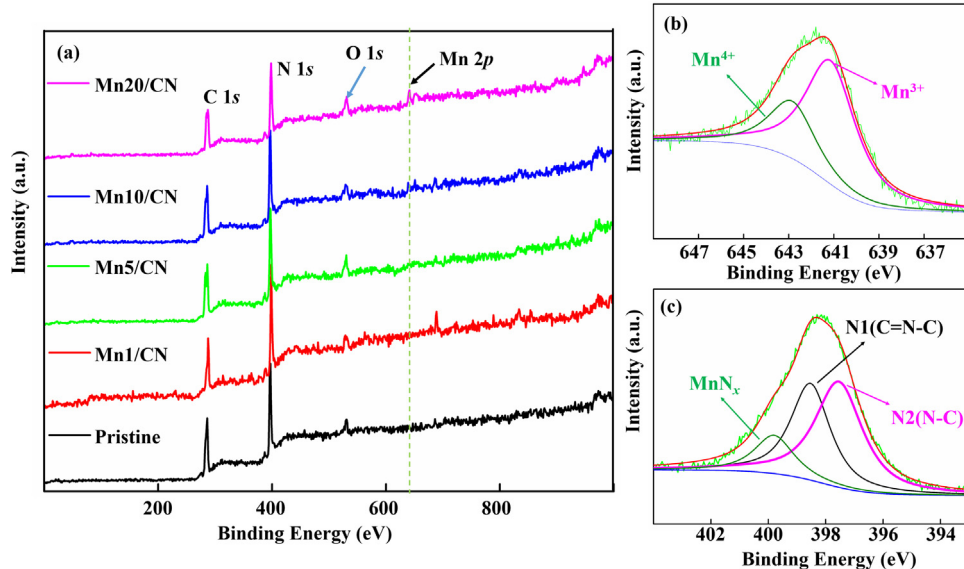


Fig. 8. XPS spectra of Mn-adsorbed g-C₃N₄, (a) survey spectra; (b) and (c) are Mn 2p_{3/2} and N 1s of Mn20/CN sample, respectively.

improve the efficiency. Therefore, the phase, particle size, and surface morphology variations are not key points for photocatalytic efficiency improvement.

3.4. Chemical composition and stability of photocatalyst

The composition and chemical status of the samples are investigated by XPS. Fig. 8(a) shows the XPS survey spectra of the pristine and the Mn-adsorbed g-C₃N₄ samples. There are only peaks of Mn, C, N and O atoms in the Mn-adsorbed g-C₃N₄ samples. The signals of Cl atoms are not observed (around 200 eV), since Cl atoms are eliminated during the heating process [37]. The atomic concentrations of Mn in the samples of Mn1/CN, Mn5/CN, Mn10/CN and Mn20/CN are 1.01, 2.70, 3.26 and 8.06 at.%, respectively. The typical high resolution XPS spectra of Mn 2p_{3/2} and N 1s peaks in the Mn20/CN are deconvoluted to show the chemical compositions, as shown in Fig. 8(b) and (c). For the deconvolution of Mn 2p_{3/2}, there are only two kinds of Mn compounds: manganese oxide (MnO_x, around 641.8 eV) and manganese nitride (MnN_x, around 640.1 eV)

[38,39] in Fig. 8(b). The proportions of MnO_x and MnN_x are 29.9 and 70.1 at.%, respectively. Fig. 8(c) shows that the XPS spectrum of N 1s in Mn20/CN is deconvoluted into three peaks centered at 397.5, 398.5 and 399.8 eV, respectively. The peaks can be attributed to the manganese nitride, N1(C=N-C) and N2(N-C), which is in accordance with the reported results [38,39]. The proportion of N in MnN_x, N1, and N2 were 14.5, 36.9, and 48.6 at.%, respectively.

XANES measurements were carried out to determine the chemical states of Mn. Fig. 9(a) presents the normalized Mn K-edge XANES spectra of Mn20/CN sample, and neat Mn₃N₂, MnN and MnO₂ for comparison. It can be observed that the position of the K-edge of Mn in the g-C₃N₄ is similar to that of MnN (6554.21 eV) and MnO₂ (6562.19 eV), locating at higher energy than that of Mn₃N₂ (6553.20 eV), which means that Mn in g-C₃N₄ is found in the trivalent and tetravalent states. The pre-edge peaks at around 6541.92 eV represent the electron transition from the 1s core levels to an unoccupied 3d levels of Mn ions, as shown in Fig. 9(b). The occurrence of a single pre-edge peak structure is associated with Mn valence state (d⁵ configuration: a dominantly tetrahedral Mn

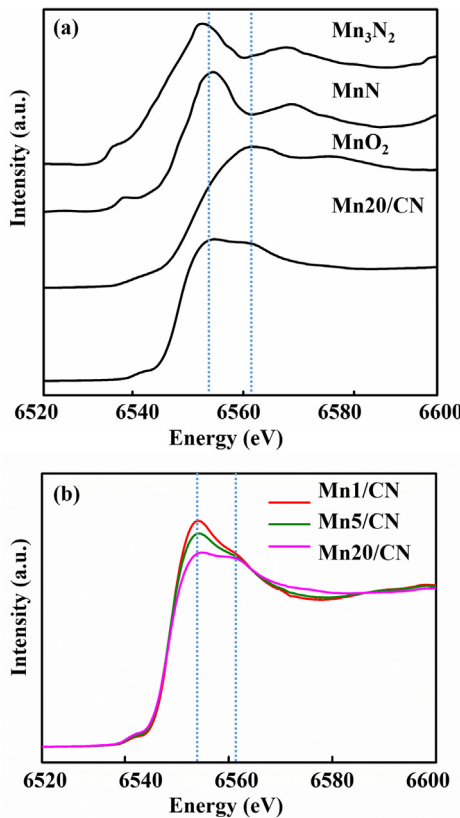


Fig. 9. (a) Mn K-edge XANES spectra of Mn20/CN, and Mn₃N₂, MnN and MnO₂ for comparison (b) Mn K-edge spectra of Mn1/CN, Mn5/CN, and Mn20/CN.

coordination), which means that the [MnN₃]^{x-} structure is dominant [40,41]. The intensity ratio of two peaks at 6554.21 (I_{Mn3+}) and 6562.19 eV (I_{Mn4+}) decreases with increasing Mn concentration, which means the ratio of Mn⁴⁺ increases with increasing Mn concentration. The coexistence of Mn³⁺ and Mn⁴⁺ indicates that the introduced Mn²⁺ has been oxidized into the higher valence state through the interaction with nitrogen or oxygen, as demonstrated in XPS.

To confirm the chemical composition changes, the adsorption energy, E_a (Mn), of a single Mn atom located at different sites on the g-C₃N₄ is calculated by using Eq. (6) [42]:

$$E_a(\text{Mn}) = [E_{m\text{Mn/g-C}_3\text{N}_4} - mE_{\text{Mn}} - E_{g\text{-C}_3\text{N}_4}] / m \quad (6)$$

where m is the number of Mn atoms. Our calculation reveal that the E_a (Mn) of Mn atoms at the T_t, N1_t, N2_t, H_t and C_t sites are -7.68, -5.77, -5.46, -5.33 and -3.27 eV, respectively. A negative value for E_a indicates that the adsorption is an exothermic reaction, while a positive value indicates that the adsorption is an endothermic reaction. Thus, Mn atoms prefer to reside over T_t (the triangular N hole positions) with the adsorption energy of -7.68 eV, which is the most stable configuration.

The type of bond between the Mn and the surface atoms is further determined by calculating the Mulliken bond population. The bond population represents the overlap degree of the electron cloud of two atoms participating in the bonding, which can be used to estimate the covalent or ionic nature of a chemical bond. The absolute value of the bond population indicates covalent or ionic bond interaction [43]. In the 1 Mn-adsorbed g-C₃N₄ system, the bond population of three Mn–N bonds are 0.32, 0.34 and 0.32 |e|, which indicates the formation of ionic bond. The Mn–N bonds in the other Mn-adsorbed g-C₃N₄ systems range from 0.10 to 0.34 |e|.

The XPS results indicate that the Mn atoms have been successfully adsorbed on the g-C₃N₄ particle, and Mn stably bonded with N atoms as MnN_x. The adsorption energy of Mn-adsorbed g-C₃N₄ is -7.68 eV, which will prevent the formation of Mn oxide, since it is necessary to acquire sufficient energy to overcome the formation energy barrier. At the same time, the bond population analysis indicates the formation of ionic bond between Mn and N atoms. Therefore, the Mn atoms can stably exist on the surface of g-C₃N₄ through the Mn–N ionic bonds and strong adsorption energy.

3.5. Optical absorption improvement

Fig. 10(a) shows the UV/vis absorption spectra of the samples. As Mn the concentration of adsorbed Mn increases, the absorption edges gradually shift to the lower energy range while the intensity of absorbance increases from 2.31 (pristine g-C₃N₄) to 2.82 (Mn20/CN). The obvious enhancement of light absorbance in the case of Mn20/CN implies that more photons are absorbed in the same irradiation condition. **Fig. 10(b)** shows the band gap of g-C₃N₄ samples calculated from the UV/vis absorption spectra. The band gaps of g-C₃N₄, Mn1/CN, Mn5/CN, Mn10/CN, and Mn20/CN are 2.93, 2.90, 2.88, 2.87, and 2.84 eV, respectively, which are in agreement with the results in the literature [44].

Fig. 10(c) shows that the excitation spectra of the g-C₃N₄ samples monitored by the emission wavelength of 460 nm. There are four broad bands in the wavelength region of 250–400 nm. As is well known, the g-C₃N₄ crystallizes in graphitic phase with space group *P-6m2* (No.187), composed of nitrogen-linked melamine units arranged in a graphite-like structure stacked in a staggered ABAB fashion. Therefore, the two excitation peaks in the region of 250–340 nm correspond to two different staggered configurations. Also, there are another two bands from 350 to 400 nm. As the absorption from C–N charge transfer transition is lower than that of the host, these two peaks originate from the C–N1 and C–N2 charge transfer transition [45,46]. These four absorption bands belong to the intrinsic properties of the compound. There is no significant change in the peak positions of the excitation spectra after Mn adsorption, which suggests that the Mn–N bonds and the crystal field strength around Mn ions are very similar to the pristine g-C₃N₄. Importantly, as the Mn concentration increases, the band from 350 to 400 nm becomes weak. As a competitive absorption of excitation light, the photon absorption from the host lattice decreases, which means the absorption from Mn atoms increases.

The inhibition of electron-hole pair recombination is known to be an important factor for improving the photocatalytic efficiency. The emission spectra originate from the recombination of electron-hole pairs, and the decreases in the emission intensity are due to the decrease of electron-hole recombination. Therefore, upon excitation of the host absorption at 274 nm, the samples show typical broad emission band in the region of 400–550 nm, peaking at around 456 nm for g-C₃N₄ (as shown in **Fig. 10(d)**), which is consistent with those reported in the literature [45,46]. In the present case, as the Mn concentration increases, the emission intensities gradually decrease, indicating that the recombination rate of electron-hole pairs decrease. Therefore, the inhibition of electron-hole recombination also plays an important role for photocatalytic efficiency improvement.

To further understand the process by which the adsorption of Mn atoms improves the photon absorption intensity, the electronic structure is investigated at an atomic level. **Fig. 11(a)** shows that the calculated band gap of g-C₃N₄ is 2.70 eV, which is smaller than our experimental results (**Fig. 10(a), (b)**). It can be seen from the PDOS that the valence band from -1.43 to 0 eV originates mainly from the N1 2p states, and the lower valence band from -3.00 to -1.43 eV derives from the hybrid of N1 2p and N2 2p states. In addition, the conduction band originates from the hybrid of N1 2p and C 2p

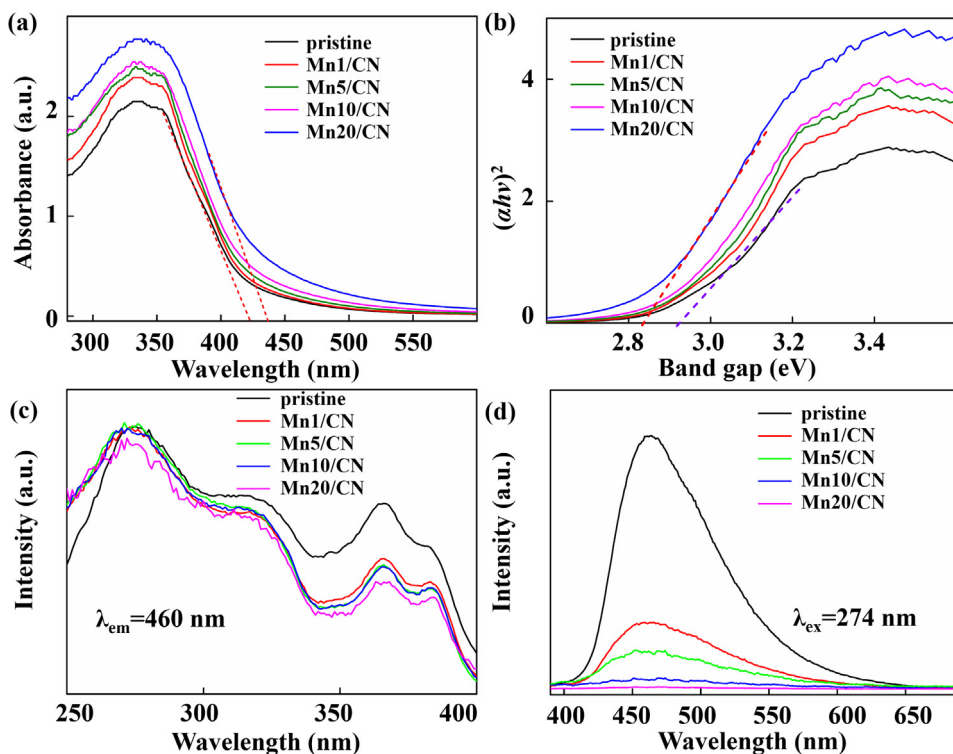


Fig. 10. (a) The UV–vis spectra, (b) estimated band gaps obtained from UV–vis spectra, (c) excitation spectra, and (d) emission spectra of pristine, Mn1/CN, Mn5/CN, Mn10/CN, and Mn20/CN.

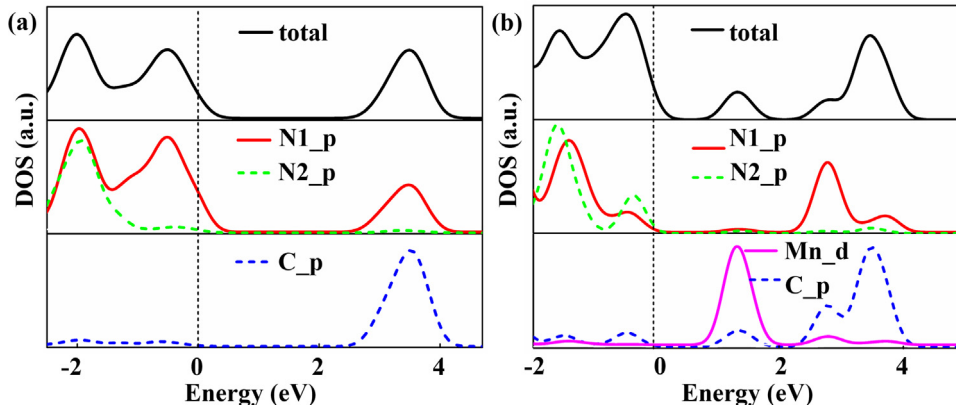


Fig. 11. (a) DOS of the pristine $\text{g-C}_3\text{N}_4$. (b) DOS of the 1 Mn-adsorbed $\text{g-C}_3\text{N}_4$. The Fermi energy is set to be 0 eV.

Table 2

The experimental and calculated band gap (E_g) and band edges (E_{VB} : the valence band edge; E_{CB} : the conduction band edge) of Mn-adsorbed $\text{g-C}_3\text{N}_4$ systems with different Mn concentrations. The unit of E_g , E_{VB} , and E_{CB} are eV.

Experiment	E_g	E_{VB}	E_{CB}	Calculation	E_g	E_{VB}	E_{CB}
$\text{g-C}_3\text{N}_4$	2.93	1.59	-1.34	$\text{g-C}_3\text{N}_4$	2.70	1.21	-1.49
Mn1/CN	2.90	1.54	-1.36	1Mn/CN	2.62	1.04	-1.58
Mn5/CN	2.88	1.48	-1.40	2Mn/CN	2.56	0.96	-1.60
Mn10/CN	2.87	1.42	-1.45	3Mn/CN	2.52	0.76	-1.76
Mn20/CN	2.84	1.25	-1.59	4Mn/CN	2.36	0.63	-1.73

states. Table 2 shows that the calculated band gap decreases with increasing Mn concentration, which is consistent with our experimental results. The decrease of the band gap is responsible for red shift of the UV–vis spectra absorption edge, inducing decrease of the excitation energy requirement of irradiated photons.

Importantly, Fig. 11(b) shows that some additional doping states emerge in the forbidden gap after Mn-adsorption. The PDOS reveals

that the doping states mainly originated from Mn 3d. In fact, the Mn 3d states play an important role in this process. These doping states divide the band gap into two parts, and offer a “bridge” for the absorption of lower energy photons. The electrons in the conduction band will be trapped by the half-filled Mn 3d state during the recombination process, which will increase the life time of photogenerated electrons and holes.

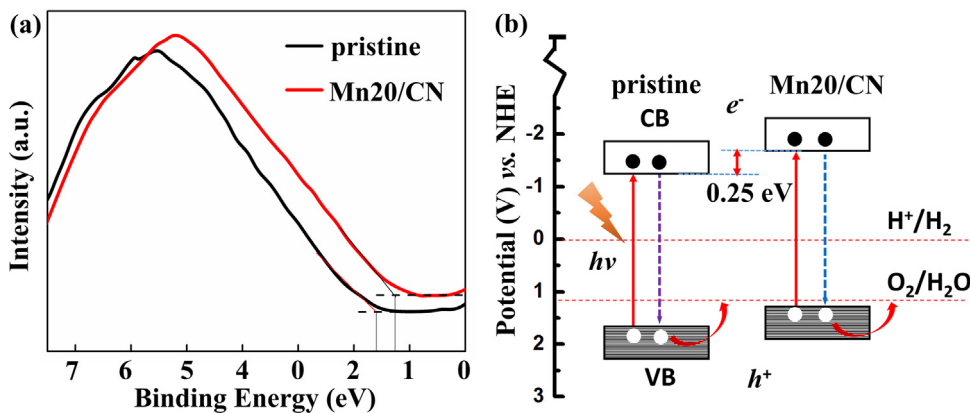


Fig. 12. (a) XPS valence band spectra of $\text{g-C}_3\text{N}_4$ and Mn20/CN, and (b) schematic illustration of the band gap structure of pristine $\text{g-C}_3\text{N}_4$ and Mn20/CN.

Table 3
The surface area and pore structure parameters of pristine and Mn-adsorbed $\text{g-C}_3\text{N}_4$.

Samples	$S_{\text{BET}}(\text{m}^2/\text{g})$	$V_{\text{Total}}(\text{cm}^3/\text{g})$	$D_{\text{Average}}(\text{nm})$
$\text{g-C}_3\text{N}_4$	21.76	0.12	21.09
Mn1/CN	21.38	0.12	18.21
Mn5/CN	22.06	0.09	17.68
Mn10/CN	22.57	0.12	23.39
Mn20/CN	24.33	0.14	21.88

3.6. Band edge shift

Our work concludes that electron-hole recombination plays an important role in photocatalytic efficiency improvement (Fig. 10(d)). In fact, many factors are thought to be responsible for the decrease of the electron-hole recombination rate, such as shape changes of the catalyst, introduction of a reaction center, or acceleration of the separation with an electric field or band edge engineering. In the present case, band edge engineering is the most likely factor. It is well known that TM-doping strongly affects the band edge of semiconductors, and the redox ability of a semiconductor is assessed by the positions of the conduction band edge (E_{CB}) and the valence band edge (E_{VB}) [46]. The E_{VB} of both pristine and Mn-adsorbed $\text{g-C}_3\text{N}_4$ samples were measured by XPS valence spectra (Fig. 12(a)). For the pristine $\text{g-C}_3\text{N}_4$, the E_{VB} is located at 1.59 eV, which is well consistent with other reports [46] while the E_{CB} would occur at about -1.34 eV according to the experimental band gap (2.93 eV). Meanwhile, for the Mn adsorbed $\text{g-C}_3\text{N}_4$, (Mn20/CN), the E_{VB} gradually shifts upwards and increases to 1.25 eV and the E_{CB} shifts up to -1.59 eV. Table 2 shows the band edge positions of different samples. To confirm the band edge position changes from experiments, DFT calculations are performed based on Eqs. (2)–(4). The results of calculated and experimental band edge are tabulated in Table 2. The band edges upshift upwards with increase in Mn concentration, which is in agreement with the experimental results. Thus, the upward shift of band edge with Mn adsorption is responsible for the photocatalyst efficiency changes.

Comparison of the experimental and calculation results reveals the tendency, and Fig. 12(b) shows a schematic illustration of the band structure of Mn-adsorbed $\text{g-C}_3\text{N}_4$ systems. The up-shifts of Fermi level of $\text{g-C}_3\text{N}_4$ with Mn concentration are due to the electron transfer from Mn to $\text{g-C}_3\text{N}_4$. As a result, the relative positions of E_{CB} and E_{VB} up-shift with the Fermi level. The up-shifting of band edges should play a crucial role in the photocatalytic process. The elevation of E_{VB} makes the photo-generated holes more easily to react with the oxygen molecules to generate superoxide ions, which will enhance the oxidation ability of holes in E_{VB} . In conclusion, the band edge up-shift after Mn adsorption is responsible for the photocatalytic efficiency improvement.

However, the photocatalytic efficiency of Mn-adsorbed $\text{g-C}_3\text{N}_4$ decreases with Mn adsorption of Mn concentration higher than Mn20/CN, which originates from the high dose manganese oxides. This reason is arrived at based on work function changes. The method of Eq. (2) is used to calculate the work functions of Mn (001) and MnO (001) to be 4.12 and 3.24 eV, respectively. The work functions of other facets of the two materials are almost similar. Due to the work functions of Mn (001) and MnO (001) being higher than that of $\text{g-C}_3\text{N}_4$ (4.36 eV), they donate electrons to $\text{g-C}_3\text{N}_4$, and result in work function upshift. With increasing Mn and MnO concentrations, the band edges further increase, and the E_{VB} shifts to be higher than the O_2 redox line. It is noteworthy that if the E_{VB} level is higher than the O_2 redox line, the photocatalytic efficiency decreases. Therefore, the photocatalytic efficiency decreases beyond the optimum Mn concentration Mn20/CN (8.06 at.%).

4. Conclusions

In this paper, a combined experimental and theoretical approach was used to identify the chemical origin of photocatalytic efficiency improvement after Mn-adsorption on $\text{g-C}_3\text{N}_4$. Due to its highest binding energy and most suitable band edge positions, Mn was chosen among the TMs as the adsorption element. Photocatalyst efficiency investigations show the noteworthy improvement of efficiency by 3 times after Mn-adsorption on $\text{g-C}_3\text{N}_4$. The phase, surface area, and surface morphology of the samples change little after Mn-adsorption, indicating that they are not the contributing factors to the improvement in efficiency. The chemical composition and corresponding electronic and optical property variations were found to be responsible for the photocatalytic efficiency improvement. The Mn atoms were found to interact with N atoms through ionic bonds, which was confirmed by the XPS, XANES, adsorption energy, and Mulliken bond population analysis. The factors for photocatalytic efficiency improvement were further investigated, and were found to mainly originate from three causes: the decrease of band gap, the introduction of half-filled Mn 3d states in the forbidden gap, and the band edge shift. Combined with UV-vis spectra and electronic structural analysis, the extension of the photon absorption range was mainly introduced from the decrease in band gap. Meanwhile, the impurity states of Mn 3d were found to increase the life time of photogenerated electrons and holes. Finally, the band edge shifts were investigated by combining the valence band XPS spectra and band edge calculations. The band edge was found to upshift with increasing Mn concentration, which could successfully inhibit the electron-hole pair recombination. In addition, the optimum concentration in our work was determined as Mn20/CN (8.06 at.%), and the reasons for the efficiency changes were investigated based on the work function difference.

Acknowledgments

This research was supported by the Basic Science Research Program through the National Research Foundation of Korea (NRF), funded by the Ministry of Education (No. 2014R1A1A2058415, No. 2015R1D1A1A01058991, and No. 2016R1A6A1A03012877), and partially supported by the China Scholarship Council (No. 201408260037).

Appendix A. Supplementary data

Supplementary data associated with this article can be found, in the online version, at <http://dx.doi.org/10.1016/j.apcatb.2017.01.034>.

References

- [1] Q.J. Xiang, J.G. Yu, M. Jaroniec, *J. Am. Chem. Soc.* 134 (2012) 6575–6578.
- [2] Y.B. Liu, G.Q. Zhu, J.Z. Gao, M. Hojamberdiev, R.L. Zhu, X.M. Wei, *Appl. Catal. B: Environ.* 200 (2017) 72–82.
- [3] C.W. Tan, G.Q. Zhu, M. Hojamberdiev, K. Okada, J. Liang, X.C. Luo, *Appl. Catal. B: Environ.* 152 (2014) 425–436.
- [4] A. Kudo, Y. Miseki, *Chem. Soc. Rev.* 38 (2009) 253–278.
- [5] B. Chai, T.Y. Peng, J. Mao, K. Li, L. Zan, *Phys. Chem. Chem. Phys.* 14 (2012) 16745–16752.
- [6] X.S. Zhou, B. Jin, R.Q. Chen, F. Peng, Y.P. Fang, *Mater. Res. Bull.* 48 (2013) 1447–1452.
- [7] L.P. Zhang, Z.H. Xia, *J. Phys. Chem. C* 115 (2011) 11170–11176.
- [8] J.S. Zhang, J.H. Sun, K. Maeda, K. Domen, P. Liu, M. Antonietti, *Energy Environ. Sci.* 4 (2011) 675–678.
- [9] Z.Y. Wang, W. Guan, Y.J. Sun, F. Dong, Y. Zhou, W.K. Ho, *Nanoscale* 7 (2015) 2471–2479.
- [10] Z.L. Ni, F. Dong, H.W. Huang, Y.X. Zhang, *Catal. Sci. Technol.* 6 (2016) 6448–6458.
- [11] F. Dong, Z.W. Zhao, Y.J. Suan, Y.X. Zhang, S. Yan, Z.B. Wu, *Environ. Sci. Technol.* 49 (2015) 12432–12440.
- [12] I.O. Maciel, J.C. Delgado, E.C. Silva, M.A. Pimenta, B.G. Sumpter, V. Meunier, *Nano Lett.* 9 (2009) 2267–2272.
- [13] D. Ghosh, G. Periyasamy, B. Pandey, S.K. Pati, *J. Mater. Chem. C* 2 (2014) 7943–7951.
- [14] C.W. Zou, L.X. Shao, L.P. Guo, D.J. Fu, T.W. Kang, *J. Cryst. Growth* 331 (2011) 44–48.
- [15] P. Choudhury, S.S. Srinivasan, V.R. Bhethanabotla, Y. Goswami, K. McGrath, E.K. Stefanakos, *Int. J. Hydrogen Energ.* 34 (2009) 6325–6334.
- [16] E. Kroke, M. Schwarz, E.H. Bordon, P. Kroll, B. Noll, A.D. Norman, *New J. Chem.* 26 (2002) 508–512.
- [17] G. Kresse, J. Furthmüller, *Phys. Rev. B* 54 (1996) 11169–11186.
- [18] A.L. Solis, I. Vasiliev, *Phys. Rev. B* 76 (2007) 235431.
- [19] B. Hammer, L.B. Hansen, J.K. Nørskov, *Phys. Rev. B* 59 (1999) 7413–7421.
- [20] S.L. Dudarev, G.A. Botton, S.Y. Sarasov, C.J. Humphreys, A.P. Sutton, *Phys. Rev. B* 57 (1998) 1505.
- [21] Y. Yang, A. Muratahan, C. Wolverton, *Phys. Rev. B* 92 (2015) 195118.
- [22] S. Grimme, *J. Comput. Chem.* 27 (2006) 1787–1799.
- [23] T.P. Hardcastle, C.R. Seabourne, R. Zan, R.M.D. Brydson, U. Bangert, Q.M. Ramasse, *Phys. Rev. B* 87 (2013) 195430.
- [24] R.D. Shannon, *Acta Cryst. A* 32 (1976) 751–767.
- [25] J.L.F.D. Silva, C. Stampfl, M. Scheffler, *Phys. Rev. Lett.* 90 (2003) 066104.
- [26] W. Zhang, Z.J. Zhang, W. Yang, J. Nanosci. Nanotechnol. 15 (2015) 8075–8080.
- [27] J.J. Liu, *J. Phys. Chem. C* 119 (2015) 28417–28423.
- [28] Y. Xu, M.A.A. Schoonen, *Am. Mineral.* 85 (2000) 543–556.
- [29] J.H. Yang, R.J. Liu, S. Huang, Y. Shao, Y. Huang, Y. Yu, *Catal. Today* 224 (2014) 104–113.
- [30] Q. Wang, C.C. Chen, D. Zhao, W.H. Ma, J.C. Zhao, *Langmuir* 24 (2008) 7338–7345.
- [31] L. Sun, Z.L. Zhao, Y.C. Zhou, L. Liu, *Nanoscale* 4 (2012) 613–620.
- [32] J. Lee, W. Choi, *J. Phys. Chem. B* 109 (2005) 7399–7406.
- [33] J.Z. Jiang, O.Y. Lei, L.H. Zhu, A.M. Zheng, J. Zou, X.F. Yi, *Carbon* 80 (2014) 213–221.
- [34] J. Rodriguez, Carvajal, July, *Fullprof*, Institute Laue-Langervin, Grenoble, France, 2006.
- [35] Z.Y. Teng, H.Y. Lv, L.N. Wang, L. Liu, C.Y. Wang, G.X. Wang, *Electrochim. Acta* 212 (2016) 722–733.
- [36] X.L. Yang, F.F. Qian, G.J. Zou, M.L. Li, J.R. Lu, Y.M. Li, *Appl. Catal. B: Environ.* 193 (2016) 22–35.
- [37] G. Amirthaganesan, T. Dhanabal, K. Nanthini, M. Dhandapani, *Mater. Lett.* 64 (2010) 264–266.
- [38] I. Matanovic, S. Babanova, A. Perry, A. Serov, K. Artyushkova, P. Atanassov, *Phys. Chem. Chem. Phys.* 17 (2015) 13235–13244.
- [39] K.L. Chao, H.Y. Liao, J.J. Shyue, S.S. Lian, *Metall. Mater. Trans. B* 45 (2014) 381–391.
- [40] E.P. Hommel, M.J. Winiarski, G. Kunert, I.N. Demchenko, O.D. Roshchupkina, J. Grenzer, V. Holy, *J. Appl. Phys.* 117 (2005) 065702.
- [41] P. Yu, J.P. Guo, L. Liu, P.K. Wang, P. Chen, *Chem. Sus. Chem.* 9 (2016) 364–369.
- [42] W.B. Zhang, S.L. Zhang, Z.J. Zhang, L.L. Wang, W. Yang, *Vacuum* 110 (2014) 62–68.
- [43] Z.C. Wu, H.L. Gao, S.C. Yan, Z.G. Zou, T. Dalton, (2014) 12013–12017.
- [44] H. Xu, J. Yan, Y.G. Xu, Y.H. Song, H.M. Li, J.X. Xia, *Appl. Catal. B: Environ.* 129 (2013) 182–193.
- [45] Q.J. Xiang, J.G. Yu, M. Jaroniec, *J. Phys. Chem. C* 115 (2011) 7355–7363.
- [46] T. Xiong, W.L. Cen, Y.X. Zhang, F. Dong, *ACS Catal.* 6 (2016) 2462–2472.